Accepted in the Journal of Micromanufacturing on 23/11/2023

Strain softening observed during nanoindentation of Equimolar-Ratio Co-Mn-Fe-Cr-Ni High Entropy Alloy

Ayush Owhal[1,2], Vinod Belwanshi[3], Tribeni Roy[1,4*] and Saurav Goel[4,5*]

[1]Birla Institute of Technology and Science Pilani, Rajasthan 333031, India
[2]Department of Mechanical Engineering, SD Bansal College, Indore, 453331, India
[3]CSIR- National Metallurgical Laboratory, Jamshedpur, India 831007
[4]London South Bank University, 103 Borough Road, London SE1 0AA, UK
[5]Department of Mechanical Engineering, University of Petroleum and Energy Studies, Dehradun, 248007, India

* Corresponding author email address: tribeni.roy@pilani.bits-pilani.ac.in; goels@lsbu.ac.uk

Abstract

This research article presents an atomistic study on the cyclic nanoindentation of equimolar-ratio Co-Mn-Fe-Cr-Ni high entropy alloy (HEA) using molecular dynamics simulation. The study investigated the effects of indentation depth on the cyclic load vs. indentation depth of the HEA. The results showed that the cyclic response exhibits a pronounced shift towards plasticity with pile-up formation instead of sinking behaviour at higher indentation depth. Within the realm of MD simulations, the simulated hardness value reached up to 16 GPa for initial indentation cycle. A steep drop in the load-displacement curve was observed during elastic-plastic transition signifying substantial strain softening of the substrate. It was found that the densely clustered stacking faults undergoes a reverse transition during cyclic loading, contributing to the back propagation phase responsible for elastic recovery, despite subsequent strain hardening. The study provides important insights into the underlying mechanisms governing the cyclic mechanical behavior of HEAs to guide their improved micromanufacturing.

Keywords: Cyclic nanoindentation, plasticity, molecular dynamics simulation, high entropy alloy, strain hardening

1. Introduction

Cantor alloys or high entropy alloys (HEAs) are a class of alloys consisting of five or more metallic elements, each with an atomic percentage ranging from 5% to 35% [1–3]. Cantor alloys can have different types of crystal structures, such as face-centered cubic (FCC), body-centered cubic (BCC), and close-packed hexagonal (HCP) [4]. The use of HEA dilutes the

needs of a particular elemental atom while providing similar or improved mechanical properties which can advance the ongoing debate and argument on reduced the need for mining. This can immensely benefit the aerospace, automotive, and biomedical industries [5]. Furthermore, the high-temperature stability and thermal shock resistance of HEA makes them a potential candidate for use in high-temperature applications [6,7]. The improved mechanical properties demonstrated by HEAs has continued to attract various research endeavours. [8]. Wu et al. [9,10] coated Fe-Co-Cr-Al-Cu-X HEA on the Cu substrate using laser high-entropy surface alloying, and the HEA coating was observed to significantly improve the hardness and the tribological performance of the material.

One of the most promising FCC-type HEAs is the Equimolar-ratio Co-Mn-Fe-Cr-Ni alloy [11]. Thermo-Calc is a widely used software used to predict phase composition of an alloy across a wide range of temperature for a wide range of compositions. **Figure 1** show the phase diagram of Co-Mn-Fe-Cr-Ni alloy obtained by calculating the Gibbs free energy at different temperature using Thermo-Calc software. It can be seen to have a narrow solidification temperature range and is single phase disordered FCC_L12 structure across a wide temperature range. At 300K, Co-Mn-Fe-Cr-Ni alloy (for equimolar ratio) has a stable FCC phase. This alloy possess remarkable low-temperature ductility, reaching ~71% at room temperature. This property makes it suitable for various applications that require high strength and toughness [12].

While there have been studies on the material design and mechanical properties of HEA systems at atomic level, there are insufficient simulation studies performed on the cyclic deformation of HEA. Cyclic loading involves repeat loading and unloading which mimics nanofatigue conditions commonly experienced by the engineering systems, which is helpful to optimise materials design.

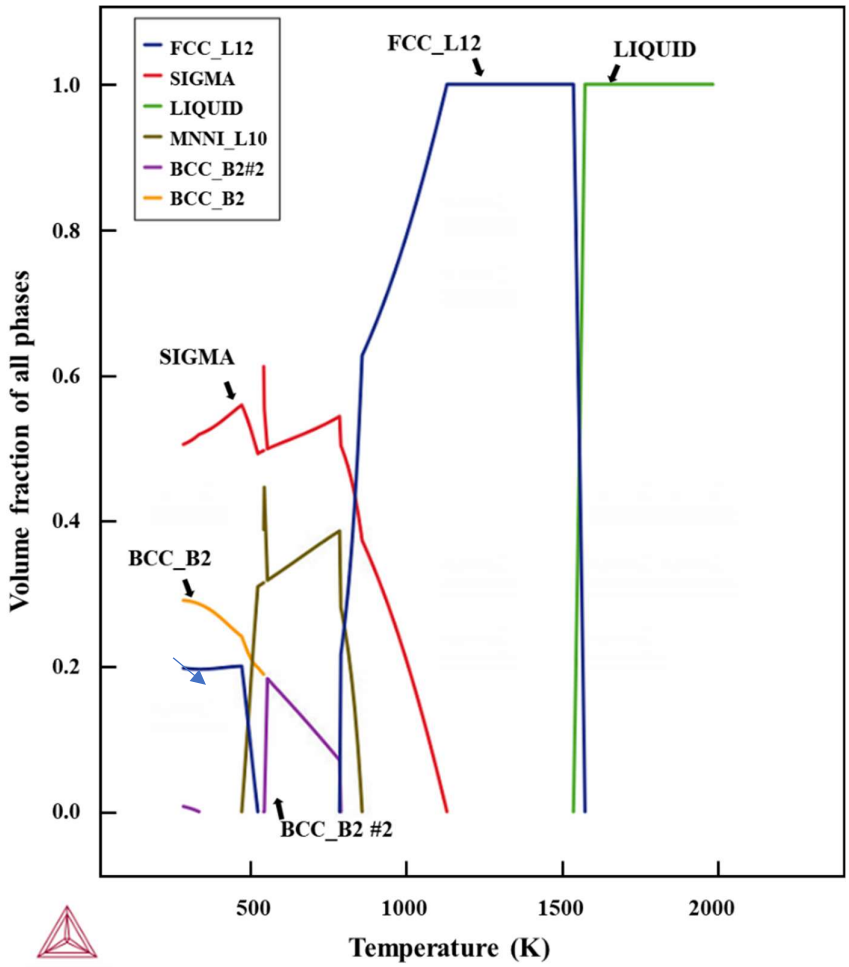

Figure 1. Thermocalc predicted phase diagram of **Co-Mn-Fe-Cr-Ni HEA** highlighting FCC phase for 0.2 mole fraction at 300 K with blue arrow.

Molecular dynamics (MD) simulation is a robust computational technique that can provide valuable insights into the mechanical behaviour of HEAs [13–15]. In the case of cyclic nanoindentation of HEAs, MD simulation can be particularly useful for understanding the underlying deformation and dislocation mechanisms. **Figure 2** highlights some key benefits of using MD simulations.

- Atomistic-level understanding: MD simulations allow researchers to observe the mechanical behaviour at the atomic level with the greatest fidelity. This atomistic-level understanding can provide valuable insights into the deformation mechanisms and dislocation behaviour of HEAs, which can be difficult to observe experimentally.
- Predicting mechanical properties: It can be used to predict the mechanical properties of HEA alloys, such as their yield strength, modulus of elasticity, and hardness. By accurately modeling the atomic interactions and deformation mechanisms, MD

simulations can provide a more comprehensive understanding of the mechanical behavior of HEAs.

- Guide for appropriate experimental work: MD simulations can provide insights that can guide experimental work. By identifying the most critical deformation mechanisms and providing detailed information on the atomic-level behavior of HEA alloys, it can inform the design of experiments and help researchers to better interpret their results.

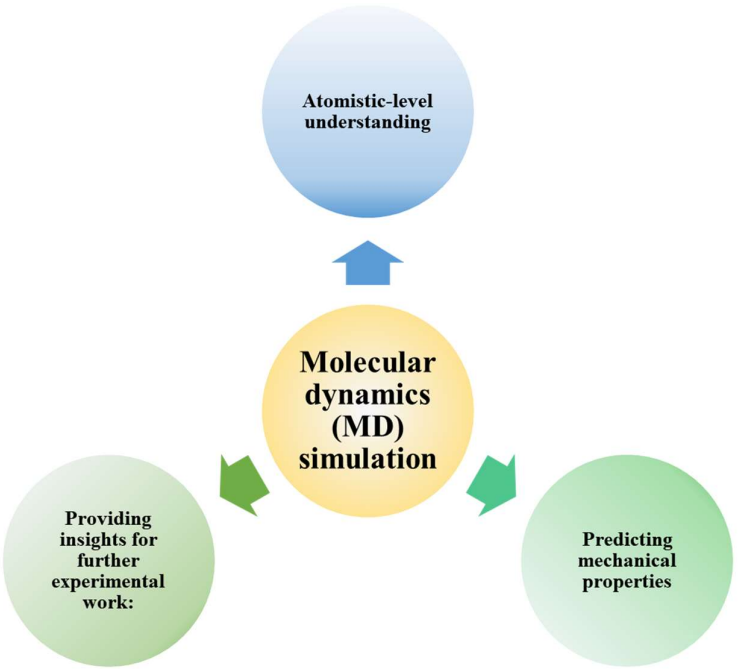

Figure 2. Key benefits of using MD simulation.

Compared to the experiments, MD simulations can aid in the real-time visualisation of the stress and strain field and slip plane evolution of the material during nanoindentation, which is convenient for in-depth understanding of the mechanical behaviour of the material. Alhafez et al. [16] conducted an MD simulation study on single nanoindentation in the equi-atomic Co-Mn-Fe-Cr-Ni Cantor alloy to understand the plasticity induced by a single nanoindentation stroke. Their work explored dislocation networks, plastic zones, and twin boundaries resulting from single nanoindentation. Recently, Fan et al. [17] used MD simulations and nanoindentation experiments to investigate hardness, modulus and dislocation mediated plasticity mechanism in Thermo-Calc phase predicted HEAs. They highlighted a “lasso” type dislocation loop due to the interaction of two shear loops on the (110) orientation. However, these studies were restricted to single stroke indentations approach. Our study seeks to offer a

holistic understanding of mechanical response of HEA by comparing single and cyclic loading conditions.

In this paper, we present a testbed study on cyclic mechanical behaviour of a representative HEA during simulated nanoindentation with specific attention made to investigate the sub-surface events.

2. Simulation methodology

In this section, the methodology for constructing a model HEA and performing cyclic nanoindentation loading tests are introduced. The details and parameters used for the model development of the MD simulation are shown in ***Table 1***.

The atomic model construction of HEA is a complex process. The two schemes available to perform this task are cluster expansion and special quasi-random structures (SQS). Of these methods, the SQS method is more popular and is implemented in software such as Atomsk which was used here in this work. Accordingly, ATOMSK [18] was used to construct the (010) oriented HEA model with an FCC lattice structure which was used as an input for the Large scale atomic/molecular massively parallel simulator (LAMMPS) [19] software. The equilibrium lattice constant of the HEA was 3.57 Å. In this alloy, all the elements were substitutionally alloyed in the Co matrix, meaning that they occupy the same crystal lattice positions as the base element. A random 80% random CO atoms were replaced by Mn, Fe, Cr, and Ni in equal ratios using ATOMSK. The simulation outputs were visualised through OVITO [20]. A schematic model of the HEA indentation process developed in this work is shown in **Figure 3**. Following the convention, the bottom most layer of the substrate was held rigidly to anchor the substate to resist the indentation force during nanoindentation and a thin thermostat was applied to mimic the experiments for taking the Joule heat away that would have otherwise been dissipated by the air surrounding the workpiece during the experiments.

Table 1: Parameters of MD simulation model to perform cyclic nanoindentation on the surface of FCC structured HEA.

Sr. No.	Parameters	Value
1	Workpiece material	HEA (Co: 20%, Mn: 20%, Fe:20%, Cr:20%, Ni:20%)
2	Lattice constant of the HEA	Face centre cubic (FCC) with a lattice constant of 3.57 Å

3	Number of atoms in the HEA substrate	8,64,000
4	Indenter	A purely repulsive indenter with a diameter of 80 Å
5	Indentation depths (*h*)	Cycle 1: 10 Å, Cycle 2: 12.5 Å, Cycle 3: 15 Å, Cycle 4: 17.5 Å and Cycle 5: 20 Å; and single shot case: 20 Å
6	Time step	2 femtoseconds
7	Initial temperature of the workpiece	300 K
8	Indenter velocity	50 m/s
9	Interatomic Potential	Second nearest neighbour modified embedded atom method (MEAM 2NN) [21]
10	Boundary	X: periodic, Y: periodic, Z: periodic

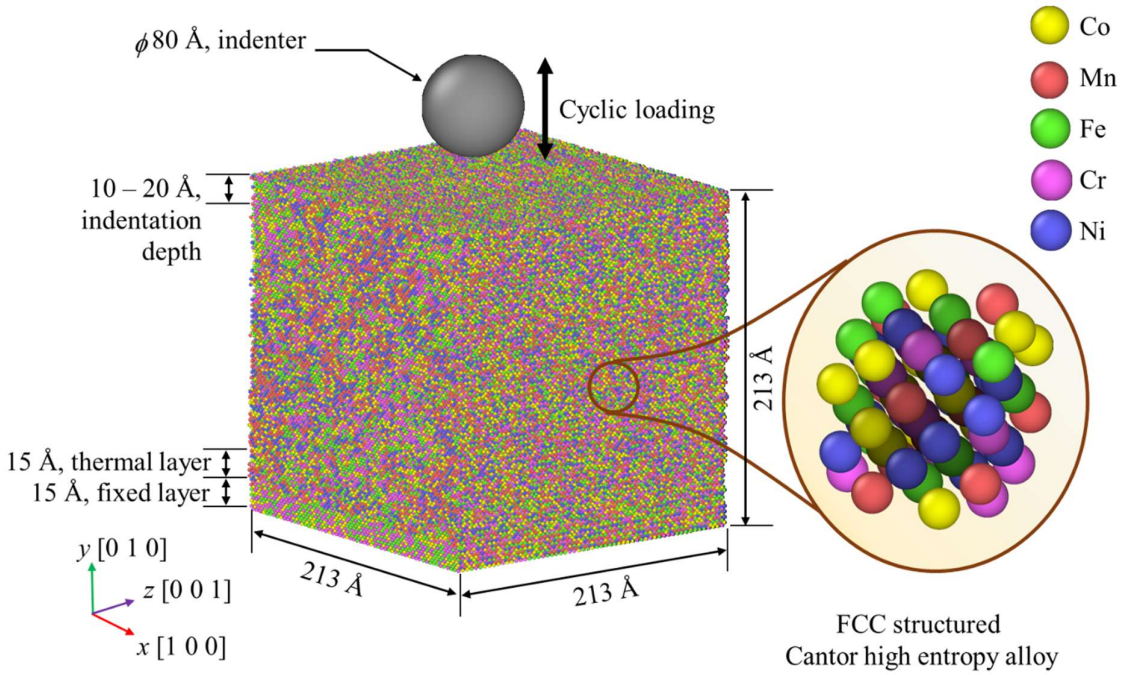

Figure 3. MD simulation model of cyclic nanoindentation. Atomic colours are shown for different elements of a model HEA system.

The second nearest neighbour modified embedded atom method (MEAM 2NN) potential was adopted to describe the chemical interactions between Co-Mn-Fe-Cr-Ni elements. This is to keep in mind that in contrast to the EAM formulation, MEAM formulation introduces an angular dependence to the electron density contribution from an atom. MEAM 2NN is an extension to the original MEAM developed by Baskes in 1992 [22], which is now referred to

as MEAM 2NN [21,23]. In this MEAM formulation, the total energy E of a system of atoms is expressed as:

$$E=\sum_i \left\{ F_i(\rho_i) + \frac{1}{2}\sum_{i\neq j} \varnothing_{ij}(r_{ij}) \right\} \quad (1)$$

where F is the embedding energy which is a function of the atomic electron density ρ, and ϕ is a pair potential interaction. The pair interaction is summed over all neighbours j of atom i within the cut-off distance, which was considered as 5 Å in this study.

An imaginary spherical shaped rigid indenter of radius, R = 40 Å was described by a repulsive force constant $F(r) = -K(r-R)^2$ where K is the force constant (1 KeV/Å^3) and r is the distance of atom of the work piece from the centre of the spherical indenter. This implies that F(r) remains repulsive if R > r or becomes zero otherwise. The HEA work sample was equilibrated for 100 ps under a constant micro-canonical ensemble (NVE)at 300 K. After the equilibration process, displacement controlled, cyclic loading was applied along the y-direction by prescribing the indenter a forward and backward cyclic velocity of 50 m/s for different time durations to achieve the intended displacement [24]. To compare the two conditions, the simulation was setup in two scenarios (i) cyclic nanoindentation with a progressive increasing displacement (indentation depth) of 10 Å (ID_{10}), 12.5 Å ($ID_{12.5}$), 15 Å (ID_{15}), 17.5 Å ($ID_{17.5}$) and 20 Å (ID_{20}); and (ii) a single shot indentation (ID_{si}) for a total indentation depth of 20 Å to benchmark against the multi-cycle indentation. The indenter was unloaded after each cyclic indentation and bring back to initial zero depth position and then reloaded to 2.5 Å deeper to previous indentation cycle. The deformation mechanisms and defect evolutions of plastic deformation were explored by the Polyhedral Template Matching (PTM).

3. Results and discussions

3.1 Response in elasto-plastic deformation regime

3.1.1 Loading and unloading response

The relation between indentation load and corresponding indentation depth in each cycle was investigated to assess the elastoplastic response at the atomic level. **Figure 4** depicts load *vs.* indentation depth (*P-h*) plots for the indentation and retraction of the indenter for both cases: cyclic and single shot indentation. Oliver and Pharr (O&P) [25] method was used to describe the elastoplastic regime and characterise the material properties for *P-h*. For elastic modulus E calculation, this method relies on the projected contact area from a power-law fitted to the

unloading curve of the *P-h* plot. The slope of unloading curve (*S*) and elastic modulus of indenter (E_i) enables one to obtain the reduced elastic modulus (E_r) of material which can then be used to obtain E using the following equations:

$$\frac{1-\upsilon^2}{E} = \frac{1}{E_r} - \frac{1-\upsilon_i^2}{E_i} \tag{2}$$

where υ and υ_i are the Poisson's ratio of work piece material and the indenter.

In this work, a rigid indenter of infinite *E* was used for indentation, thus, *E* of HEA system can be calculated using formula:

$$E = E_r \times (1-\upsilon^2) \tag{3}$$

where the value of υ (Poisson's ratio of Co-Mn-Fe-Cr-Ni HEA) was taken as 0.265 from the previous study [26]. Thus, E_r can be obtained as:

$$E_r(in\ GPa) = \frac{1}{\beta}\frac{\sqrt{\pi}}{2}\frac{S}{\sqrt{A_c}} \tag{4}$$

where β (1 for spherical indenter) is a constant, A_c ($= \pi h(2r-h)$) is projected contact area (m^2), *S* is the slope of the top one-third part of the unloading curve which was obtained as 855 N/m for initial indentation depth of 10 Å from the simulation result.

The obtained value of E_r from O&P equation was ≈ 161 GPa and this value was used to obtain *E* of HEA from Eq. 3 as ≈150 GPa for the [0 1 0] crystal orientation. It must however be noted that the purely repulsive indenter has limitations and does often less accurate values for the hardness and modulus which has been discussed extensively in our other work [27].

Moreover, for the known E_r value, a Hertzian power law [28] curve can be plotted to distinguish the elastic regime under a spherical nanoindentator using:

$$P = \frac{4}{3}E_r R^{1/2} h^{3/2} \tag{5}$$

where *R* is the indenter radius.

During the initial indentation at depth 10 Å, the HEA system demonstrated a close match between its elastic regime and the Hertzian fit, up to a peak load of 326 nN (~ depth of 8.6 Å) which is also shown in **Figure 4**. This peak load marks the critical transition point from elastic to plastic behavior, indicating the limit of material's elastic regime under the finite indenter size used. Beyond this point, plastic flow begins. It is worth noting that after the first indentation, nearly all subsequent cycles exhibited a strain hardening effect, indicating the formation of a restrictive disordered crystallography resulting from deformation-induced hardening. These effects were particularly prominent in $ID_{12.5}$ and ID_{20} cycles at depths of 7.5 Å and 13 Å,

respectively. Interestingly in the case of ID_{si}, strain hardening was observed to occur after significant plastic flow before the onset of strain hardening during single shot indentation compared to the cyclic nanoindentation. When examining the plastic regime of ID_{si}, the loading response closely aligned with the cyclic loading responses up to a depth of 17.5 Å. However, beyond that depth, ID_{20} cycle exhibited an increase in loading force, reaching 610 nN, whereas the ID_{si} case only reached 502 nN for the same depth of 20 Å.

The observed hysteresis in the P-h plots for all nanoindentation cases exhibit a trend that was consistent with previous experimental and computational studies [16,29,30]. Apart from shallow indentation in the ID_{10} cycle, a reverse load was observed at the beginning of unloading in subsequent cycles, including the ID_{si} case at a depth of 20 Å. This phenomenon may be attributed to the existence of sunken disordered crystallography and entanglement at deeper indentation with strain hardening, exerting force on the indenter during the elastic recovery phase.

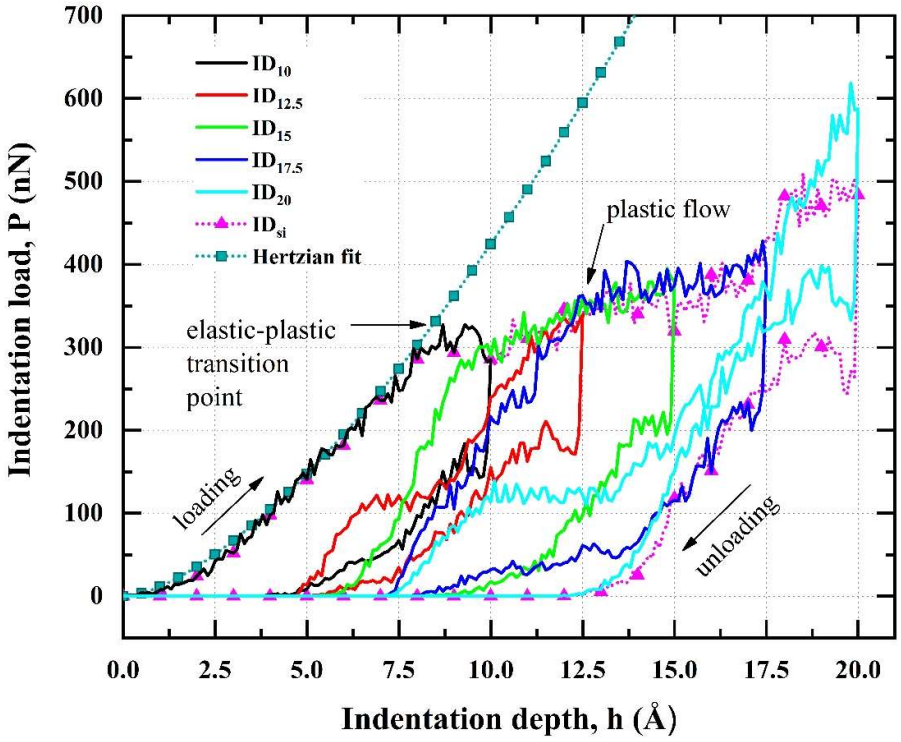

Figure 4. Simulated load *vs.* indentation depth obtained from indentation-retraction cycles for the **Co-Mn-Fe-Cr-Ni** HEA system. The unloading slope provides an E_r of ≈ 161 GPa, which was used to fit the Hertzian law ($P=4/3\ E_rR^{1/2}h^{3/2}$). A single shot indentation is shown in dashed magenta line.

3.1.2 Resistance to plastic deformation regime

The response of cyclic loading on the hardness of metals in the plastic deformation regime can be obtained from the P-h plot shown in **Figure 5a**. Hardness values in this study were determined using the ratio of the indentation load to the geometric projected contact area under the indenter at a finite depth of indentation. During the loading phase, fluctuations in hardness were observed, primarily attributed to atomic reconfiguration triggered by an avalanche of stacking faults and strain hardening phenomena. Notably, the strain hardening effect observed in the hardness versus indentation depth curves during both cyclic and single shot indentation experiments exhibit a resemblance to the observations made in the *P-h* plots.

The hardness values obtained during cyclic nanoindentation exhibited intriguing variations, as shown in **Fig 5a**. The initial increase in the load (for all the cycles) can be attributed to elastic deformation, whereas once the peak load is reached, the load decreases due to the strain softening behaviour. To quantify this, the hardness was calculated after each indentation cycle which is shown in **Fig 5b**. It can be seen from these hardness variations that Cycle 2 and Cycle 5 showed a reduced value corroborating with the hypothesis that the HEA has undergone strain softening.. The initial indentations in the ID_{10} and ID_{si} cases exhibited a peak hardness of approximately 16 GPa at the elastic-plastic transition point, with an average hardness of 15.2 ± 0.8 GPa for ID_{10} and 13 ± 1.4 GPa for ID_{si}. These hardness values obtained for the HEA system were found to be higher than experimental values [31] attributed to the use of a purely repulsive indenter and small size of the indentation[27]. Moreover, it is important to consider the size effect when interpreting the results of shallow indentations. The size effect refers to the phenomenon where the mechanical response of a material is influenced by the scale of deformation.

After ID_{10} cycle, a notable decrease of 42.7% in the average hardness was observed compared to the $ID_{12.5}$ cycle. Subsequently for ID_{15} cycle, the average hardness increased to 13 ± 0.6 GPa. However, this trend again reversed to an average hardness of 8.2 ± 3.7 GPa for ID_{20}. The observed variations in the average hardness may be attributed to pile-up formation, which influences the contact area. Moreover, the elastic recovery of the material between successive cycles contribute to the observed fluctuations in hardness. The subsequent increase in average hardness during the ID_{15} cycle, followed by another decrease in subsequent cycles, suggests the presence of additional deformation mechanisms at higher depths. To gain a comprehensive understanding of these hardness variations during cyclic nanoindentation, further investigations were necessary to elucidate the underlying mechanisms involved.

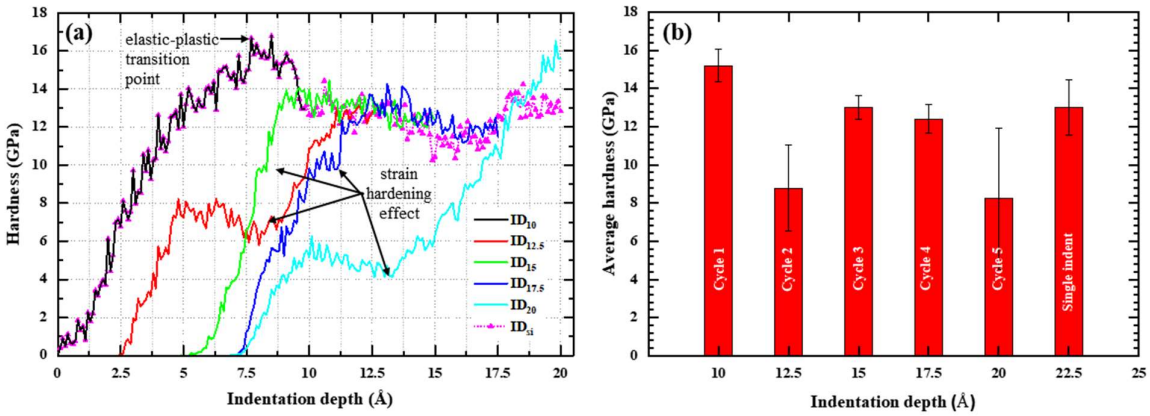

Figure 5. (a) Hardness *vs.* indentation plots for elastoplastic regime during loading phase of nanoindentation and (b) representative average hardness *vs.* indentation depth within the plastic deformation regime.

3.2 Analysis of atomistic simulations

3.2.1 Out-of-plane atomic displacement profile analysis

Fig 6 presents a topographic analysis of the indented HEAat various stages of loading and unloading for different depths of indentation. For ID_{10} cycle, out-of-plane atomic displacement was observed. However, up to depth of 12.5 Å height of pile up was insignificant to understand the type of profiles.

As the indentation depth increased in subsequent cycles, starting from ID_{15}, clear pile-up profiles were observed in the (010) crystallographic direction, exhibiting a four-fold symmetry in retraction. It is to be noted that the maximum pile-up profiles of height ≈ 5 Å was observed for ID_{20} retraction compared to ≈ 4.1 Å for ID_{si} retraction. These out-of-plane pile-up profiles suggests restricted in-plane atomic displacements of the material accompanied by significant plastic flow. The pronounced plastic flow of the material, as evidenced by the pile-up formations, contribute to the variations in average hardness during cyclic nanoindentation. These phenomena in HEA system can confer notable advantages in the realm of micromachining such materials. This stems from the potential effects induced by pile up on the precise execution of machining operations, the quality of the resulting surface, and the forces exerted during cutting processes.

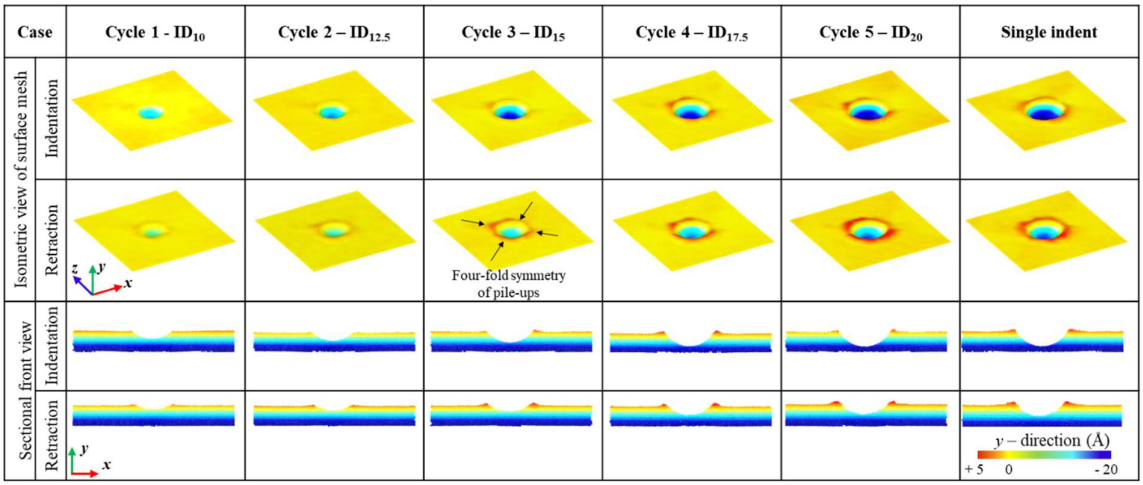

Figure 6. Schematic of atomic displacement profiles after indentation and retraction cycles at indentation depth from 10 Å to 20 Å on HEA system. The depth in y-direction is represented by rainbow colours. The out-of-plane pile-ups appear in red colour. To understand the indentation, the depth in the sectional views of geometry is sliced in y-direction up to 25 Å depth.

3.2.2 Analysis of stacking fault evolution and structural changes

Stacking faults (SFs) play a significant role in the strain hardening effect and pile-up formation observed during nanoindentation of crystalline materials [32]. SFs are deviations from the ideal atomic arrangement within the crystal lattice, causing disruptions in the sequential stacking of atomic layers. These SFs have a profound impact on the strain field around the indentation and influence the elasto-plastic deformation behavior [24].

The SFs evolution in FCC structured HEA during the nanoindentation process is shown in **Figure 7(a-c).** Form **Figure 7a,** stacking faults with a V-shaped arrangement beneath the shallow indentation were observed, serving as slip planes for dislocation movement during initial plastic deformation.

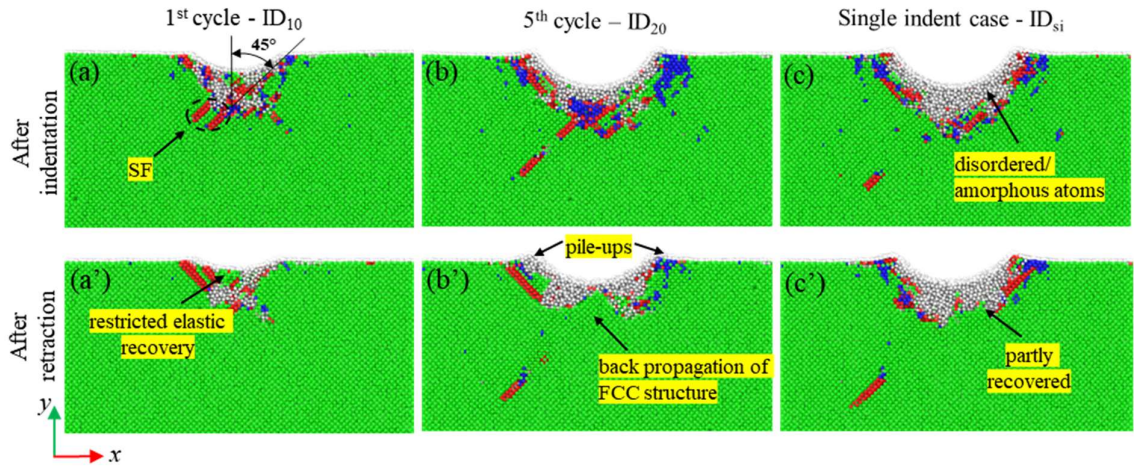

Figure 7. Snapshots of sectional view of the evolution of stacking fault structures during indentation and retraction (') cycle of (b) ID_{10}, (c) ID_{20}, and (d) ID_{si}. Atoms are coloured as per the structure type; FCC, BCC, HCP, and disordered structure in green, red, blue, and grey colour, respectively. Besides, the figure size does not represent the actual model size.

At higher indentation depths, clustering of SF inhibits dislocation motion and contributes to strain hardening effects. During the retraction cycle, these SFs restrict elastic recovery. It can be noted that after the 5th cycle of indentation (ID_{20}), reduced SF-mediated disordered structure were observed compared to single-shot indentation (**Figure 7b and c**).

Figure 8 depicts defect formations after indentation and retraction for ID_{10}, ID_{20} and ID_{si} cases, providing further insights into the evolution of stacking faults. During the initial cycle of indentation, marked by a shallow depth of 10 Å, the onset of plasticity beneath the indenter can be seen. The network density of SF structures near the indenter tip was increased in the 5th cycle of indentation compared to 1st cycle, which hinders elastic recovery. It was found that densely clustered SF undergoes reverse transition during cyclic loading, which contributed to reversible FCC ordering or back propagation, as observed in **Figure 7b'**. This was in contrast to the single shot indent which showed wider SF formation that hinders such back propagation and recovery. Furthermore, the formation of clustered SF was primarily responsible for early strain hardening in cyclic loading. As a result, the average hardness values were higher in cyclic loading cases compared to single-shot indentations.

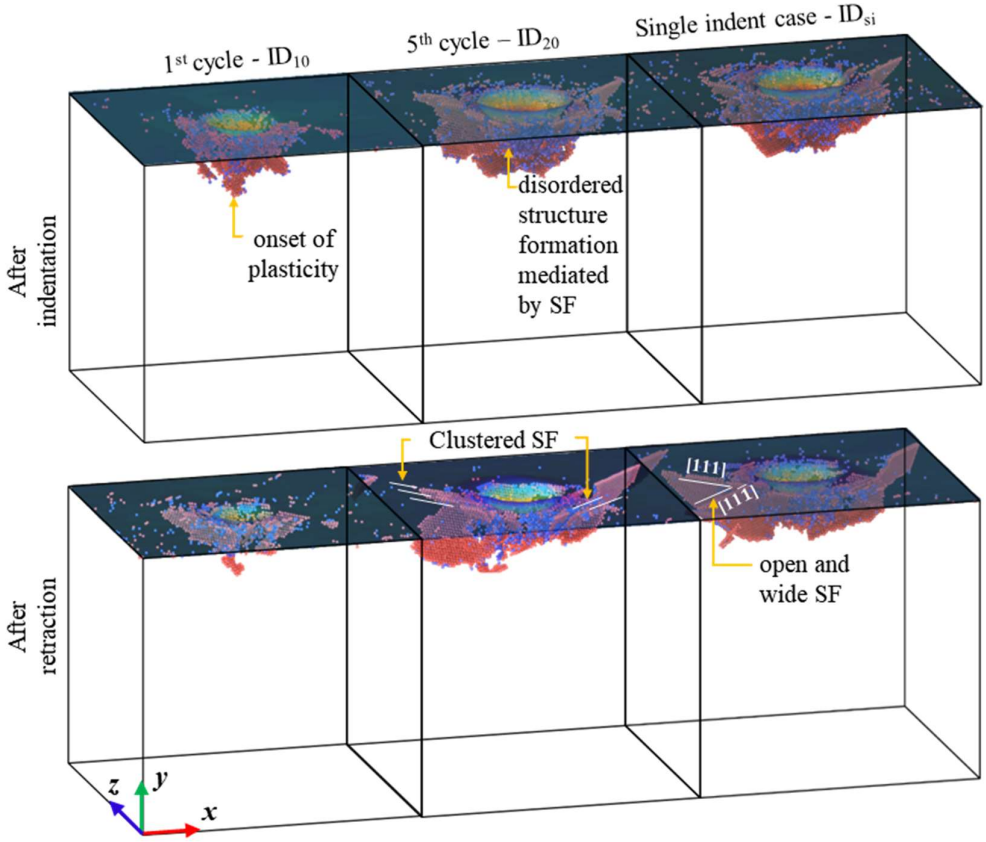

Figure 8. The snapshots of crystal defect in ID_{10}, ID_{20}, and ID_{si} case after indentation and retraction of indentation. Noting that all FCC atoms have been deleted, leaving red BCC that denote the stacking faults or twin boundary and blue HCP formations.

3.3 Elastic recovery analysis

During cyclic nanoindentation, elastic recovery plays a crucial role in mitigating inelastic deformations and enabling the material to partially restore its initial state, as illustrated in **Figures 7** and **8**. This phenomenon contributes to the material's resilience and its ability to withstand repeated loading cycles. Elastic recovery also influence the formation of pile up and affects hardness. To analyze the elastic depth recovery, an evaluation was conducted from position of surface atoms. The percentage of elastic depth recovery ratio was determined using **Eq. 3** [33] and presented in **Figure 9**.

$$Elastic\ recovery\ (\%),\ h_{re} = \frac{(h-h')}{h} \times 100, \tag{5}$$

where h is maximum indentation depth, h' unrecovered depth after retraction.

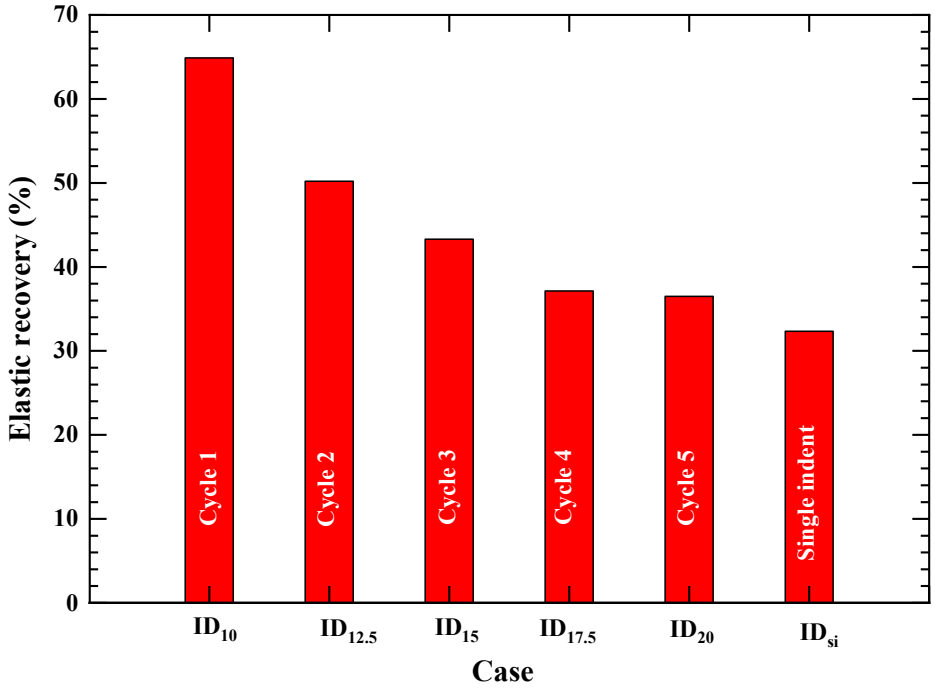

Figure 9. Elastic depth recovery for observed in cyclic and single shot nanoindentation cases.

In the 1st cycle, which had a shallow indentation depth of 10 Å, the process primarily remained in the elastic regime without significant disruption of crystallography. As a result, the obtained recovery was maximum with a depth recovery of 64.8%, as shown in **Figure 9**. Subsequent cycles with higher indentation depths exhibited inelastic behavior, leading to a decreasing trend in the elastic depth recovery ratio. Here, the intermediate cycles of $ID_{12.5}$, ID_{15}, and $ID_{17.5}$ showed elastic depth recovery ratios of 50.2%, 43.3%, and 37.14%, respectively. This decrease was attributed to strain hardening and an extended plastic regime at higher indentation depths, resulting in lower elastic depth recovery. In the final cycle of ID_{20}, an elastic depth recovery of 36.5% was observed, which was 13% higher than the 32.3% recovery observed in the single-shot indentation case with the same depth. These findings are consistent with the observations from the previous section, suggesting that cyclic loading promotes a higher degree of recovery due the FCC back propagation phase responsible for the elastic recovery despite of strain hardening.

The elastic behaviour of HEA in cyclic nanoindentation is relevant to micromachining processes as it helps mitigate permanent deformations and facilitates material recovery, contributing to precision, reduced damage, and improved efficiency in microscale manufacturing.

4. Conclusion

This atomistic study investigated the effects of indentation depth on the cyclic mechanical behaviour of a model HEA (Co-Mn-Fe-Cr-Ni). The results revealed a pronounced degree of pile-up formation at higher indentation depths, accompanied by strain hardening due to restricted atomic displacements on slip planes. The initial indentations at 10 Å depth showed strong size effects resulting in an estimated hardness of approximately 16 GPa at the elastic-plastic transition point. A phenomenon of strain hardening was observed as the plastic deformation starts, which can be attributed to the restricted atomic displacements on the slip planes. Despite undergoing strain hardening, densely clustered SF was found to undergo a reverse transition during cyclic loading, contributing to the back propagation phase responsible for elastic recovery. These findings provide valuable insights for improving micromanufacturing processes, enhancing precision, reducing damage, and increasing efficiency in microscale manufacturing applications with HEAs.

Acknowledgements:

The authors would like to acknowledge the financial support provided by the UKRI via Grants No. EP/S036180/1 and EP/T024607/1, feasibility study award from the UKRI National Interdisciplinary Circular Economy Hub (EP/V029746/1), the Hubert Curien Partnership award 2022 from the British Council and the International exchange Cost Share award by the Royal Society (IEC\NSFC\223536). Additionally, we are gratefully thankful for receiving access to various HPC resources including the Isambard Bristol, UK supercomputing service as well as Kittrick (LSBU) and Param Ishan (IIT Guwahati, India).

Data statement:

The raw data being reported in this paper can be obtained from the corresponding author upon reasonable request.

Declarations

The authors declare that they have no known competing financial interests or personal relationships that could have appeared to influence the work reported in this paper.

References

[1] B. Cantor, I.T.H. Chang, P. Knight, A.J.B. Vincent, Microstructural development in equiatomic multicomponent alloys, Mater. Sci. Eng. A. 375–377 (2004) 213–218. https://doi.org/10.1016/j.msea.2003.10.257.

[2] P. Fan, N.K. Katiyar, X. Zhou, S. Goel, Uniaxial pulling and nano-scratching of a newly synthesized high entropy alloy, APL Mater. 10 (2022) 111118. https://doi.org/10.1063/5.0128135.

[3] N.K. Katiyar, G. Goel, S. Goel, Emergence of machine learning in the development of high entropy alloy and their prospects in advanced engineering applications, Emergent Mater. 4 (2021) 1635–1648. https://doi.org/10.1007/s42247-021-00249-8.

[4] S. Singh, N.K. Katiyar, S. Goel, S.N. Joshi, Phase prediction and experimental realisation of a new high entropy alloy using machine learning, Sci. Rep. 13 (2023) 4811. https://doi.org/10.1038/s41598-023-31461-7.

[5] S. Xiang, H. Luan, J. Wu, K.-F. Yao, J. Li, X. Liu, Y. Tian, W. Mao, H. Bai, G. Le, Q. Li, Microstructures and mechanical properties of CrMnFeCoNi high entropy alloys fabricated using laser metal deposition technique, J. Alloys Compd. 773 (2019) 387–392. https://doi.org/10.1016/j.jallcom.2018.09.235.

[6] L. Yao, J. Ao, M. Jeng, J. Bi, S. Gao, Q. He, Z. Zhou, G. Sun, Y. Sun, L. Chang, J. Chen, CZTSe solar cells prepared by electrodeposition of Cu / Sn / Zn stack layer followed by selenization at low Se pressure, (2014) 1–11.

[7] Z. Qiu, C. Yao, K. Feng, Z. Li, P.K. Chu, Cryogenic deformation mechanism of CrMnFeCoNi high-entropy alloy fabricated by laser additive manufacturing process, Int. J. Light. Mater. Manuf. 1 (2018) 33–39. https://doi.org/10.1016/j.ijlmm.2018.02.001.

[8] F. Otto, A. Dlouhý, C. Somsen, H. Bei, G. Eggeler, E.P. George, The influences of temperature and microstructure on the tensile properties of a CoCrFeMnNi high-entropy alloy, Acta Mater. 61 (2013) 5743–5755. https://doi.org/10.1016/j.actamat.2013.06.018.

[9] C.L. Wu, S. Zhang, C.H. Zhang, H. Zhang, S.Y. Dong, Phase evolution and properties in laser surface alloying of FeCoCrAlCuNi high-entropy alloy on copper substrate, Surf. Coatings Technol. 315 (2017) 368–376. https://doi.org/10.1016/j.surfcoat.2017.02.068.

[10] C.L. Wu, S. Zhang, C.H. Zhang, J. Chen, S.Y. Dong, Phase evolution characteristics and corrosion behavior of FeCoCrAlCu-X 0.5 coatings on cp Cu by laser high-entropy alloying, Opt. Laser Technol. 94 (2017) 68–71.

https://doi.org/10.1016/j.optlastec.2017.03.023.

[11] B. Gludovatz, A. Hohenwarter, K.V.S. Thurston, H. Bei, Z. Wu, E.P. George, R.O. Ritchie, Exceptional damage-tolerance of a medium-entropy alloy CrCoNi at cryogenic temperatures, Nat. Commun. 7 (2016) 10602. https://doi.org/10.1038/ncomms10602.

[12] Y. Zhang, T.T. Zuo, Z. Tang, M.C. Gao, K.A. Dahmen, P.K. Liaw, Z.P. Lu, Microstructures and properties of high-entropy alloys, Prog. Mater. Sci. 61 (2014) 1–93. https://doi.org/10.1016/j.pmatsci.2013.10.001.

[13] T.L. Dora, A. Owhal, T. Roy, S.U. Belgamwar, S. Goel, H.Y. Nezhad, R.R. Mishra, Thermo-physical characteristics of 3C-SiC structure subjected to microwave exposure: A molecular dynamics study, Mater. Today Commun. 35 (2023) 105693. https://doi.org/10.1016/j.mtcomm.2023.105693.

[14] H. Sharma, A. Owhal, D. Gautam, S. Shrivastava, J.S. Rathore, S.U. Belgamwar, V.K.P. Rao, Thermoatomic analysis of monovacancy defected single-walled boron nitride nanotube under quasi-static strain: Insights from molecular dynamics, Mater. Chem. Phys. 294 (2023) 127020. https://doi.org/10.1016/j.matchemphys.2022.127020.

[15] A. Owhal, D. Gautam, S.U. Belgamwar, V.K.P. Rao, Atomistic approach to analyse transportation of water nanodroplet through a vibrating nanochannel: scope in bio-NEMS applications, Mol. Simul. (2022) 1–8. https://doi.org/10.1080/08927022.2022.2052065.

[16] I. Alabd Alhafez, C.J. Ruestes, E.M. Bringa, H.M. Urbassek, Nanoindentation into a high-entropy alloy – An atomistic study, J. Alloys Compd. 803 (2019) 618–624. https://doi.org/10.1016/j.jallcom.2019.06.277.

[17] P. Fan, N.K. Katiyar, M. Arshad, M. Bai, H. Mao, S. Goel, Anisotropic plasticity mechanisms in a newly synthesised high entropy alloy investigated using atomic simulations and nanoindentation experiments, J. Alloys Compd. 970 (2024) 172541. https://doi.org/10.1016/j.jallcom.2023.172541.

[18] P. Hirel, Atomsk: A tool for manipulating and converting atomic data files, Comput. Phys. Commun. 197 (2015) 212–219. https://doi.org/10.1016/j.cpc.2015.07.012.

[19] S. Plimpton, LAMMPS-large-scale atomic/molecular massively parallel simulator, Sandia Natl. Lab. (2007).

[20] A. Stukowski, Visualization and analysis of atomistic simulation data with OVITO–the Open Visualization Tool, Model. Simul. Mater. Sci. Eng. 18 (2009) 015012. https://doi.org/10.1088/0965-0393/18/1/015012.

[21] B.-J. Lee, M.I. Baskes, H. Kim, Y. Koo Cho, Second nearest-neighbor modified embedded atom method potentials for bcc transition metals, Phys. Rev. B. 64 (2001) 184102. https://doi.org/10.1103/PhysRevB.64.184102.

[22] M.I. Baskes, Modified embedded-atom potentials for cubic materials and impurities, Phys. Rev. B. 46 (1992) 2727–2742. https://doi.org/10.1103/PhysRevB.46.2727.

[23] B.-J. Lee, M.I. Baskes, Second nearest-neighbor modified embedded-atom-method potential, Phys. Rev. B. 62 (2000) 8564–8567. https://doi.org/10.1103/PhysRevB.62.8564.

[24] A.B. Shinde, A. Owhal, A. Sharma, P. Ranjan, T. Roy, R. Balasubramaniam, Comparative analysis of mechanical properties for mono and poly-crystalline copper under nanoindentation – Insights from molecular dynamics simulations, Mater. Chem. Phys. 277 (2022) 125559. https://doi.org/10.1016/j.matchemphys.2021.125559.

[25] W.C. Oliver, G.M. Pharr, An improved technique for determining hardness and elastic modulus using load and displacement sensing indentation experiments, J. Mater. Res. 7 (1992) 1564–1583. https://doi.org/10.1557/JMR.1992.1564.

[26] A. Haglund, M. Koehler, D. Catoor, E.P. George, V. Keppens, Polycrystalline elastic moduli of a high-entropy alloy at cryogenic temperatures, Intermetallics. 58 (2015) 62–64. https://doi.org/10.1016/j.intermet.2014.11.005.

[27] S. Goel, G. Cross, A. Stukowski, E. Gamsjäger, B. Beake, A. Agrawal, Designing nanoindentation simulation studies by appropriate indenter choices: Case study on single crystal tungsten, Comput. Mater. Sci. 152 (2018) 196–210. https://doi.org/10.1016/j.commatsci.2018.04.044.

[28] H. Hertz, Ueber die Berührung fester elastischer Körper., Crll. 1882 (1882) 156–171. https://doi.org/10.1515/crll.1882.92.156.

[29] L.L. Xiao, Z.Q. Zheng, S.W. Guo, P. Huang, F. Wang, Ultra-strong nanostructured CrMnFeCoNi high entropy alloys, Mater. Des. 194 (2020) 108895. https://doi.org/10.1016/j.matdes.2020.108895.

[30] S. Sinha, R.A. Mirshams, T. Wang, S.S. Nene, M. Frank, K. Liu, R.S. Mishra, Nanoindentation behavior of high entropy alloys with transformation-induced plasticity, Sci. Rep. 9 (2019) 6639. https://doi.org/10.1038/s41598-019-43174-x.

[31] X. Fan, R. Qu, Z. Zhang, Relation Between Strength and Hardness of High-Entropy Alloys, Acta Metall. Sin. (English Lett. 34 (2021) 1461–1482. https://doi.org/10.1007/s40195-021-01252-y.

[32] D.P. Ranjan, M.A. Owhal, D. Chakrabarti, D.S. Belgamwar, T. Roy, D.R.

Balasubramaniam, Fundamental Insights of Mechanical Polishing on Polycrystalline Cu Through Molecular Dynamics Simulations, SSRN Electron. J. (2022). https://doi.org/10.2139/ssrn.4062796.

[33] J. Li, B. Lu, Y. Zhang, H. Zhou, G. Hu, R. Xia, Nanoindentation response of nanocrystalline copper via molecular dynamics: Grain-size effect, Mater. Chem. Phys. 241 (2020) 122391. https://doi.org/10.1016/j.matchemphys.2019.122391.